Volume 54
Number 43
21 November 2025
Pages 15935-16256

Dalton Transactions

An international journal of inorganic chemistry

rsc.li/dalton

ISSN 1477-9226

ROYAL SOCIETY OF CHEMISTRY

PAPER

Takumi Masuda, Yasushi Sekine *et al.*
Porous silica materials derived from cage-siloxane: structural confinement and stabilisation of dispersed Au(0) nanoparticles

Dalton Transactions

PAPER

View Article Online
View Journal | View Issue

Cite this: *Dalton Trans.*, 2025, **54**, 15991

Porous silica materials derived from cage-siloxane: structural confinement and stabilisation of dispersed Au(0) nanoparticles

Takumi Masuda,[a] Takuya Hikino,[b,c] Rei Umeda,[a] Atsushi Shimojima[a,c,d] and Yasushi Sekine *[a,c,d]

Received 31st July 2025,
Accepted 15th September 2025

DOI: 10.1039/d5dt01824b

rsc.li/dalton

Highly dispersed gold(Au) species exhibit unique catalytic properties that differ considerably from those of bulk Au or larger particles. However, achieving such dispersion while preserving their intrinsic characteristics remains a challenge. This difficulty often arises because conventional methods can alter the characteristics of the Au itself. This study addresses this issue using silica, a support material known for its weak interaction with active metal species. Specifically, we developed a novel nanoporous silica support functionalised with hydrosilyl groups using a cage-siloxane as a building block. These groups enable on-site reduction of Au^{3+} ions, allowing highly dispersed Au loading without introducing strongly interacting ligands. Importantly, the dispersion was retained even after calcination, indicating a confinement effect within the porous structure. This approach offers a promising strategy for stabilising Au species on inert supports, potentially advancing the design of robust and efficient Au-silica catalysts for heterogeneous catalysis.

Introduction

Gold (Au) has attracted considerable attention as a catalytic material since the pioneering discoveries reported by Haruta[1] and Hutchings,[2] whose work revealed that Au nanoparticles (NPs) exhibit unexpectedly high catalytic activity. In such systems, the particle size and dispersion of Au NPs are key determinants of catalytic performance.[1,3,4] However, controlling both parameters on conventional supports remains as a formidable challenge. Reducible oxides (*e.g.*, TiO_2, ZrO_2, CeO_2) can often facilitate the deposition of small Au NPs mainly through deposition–precipitation methods,[4] whereas "inert" silica supports,[5] which are valued for their thermal and chemical robustness,[6,7] interact only weakly with Au,[7,8] typically leading to poor dispersion and facile aggregation of metallic NPs.[4–7]

Various approaches reportedly improve the dispersion of Au NPs on silica: the introduction of heteroatom dopants or partial modification with other oxides,[9] use of gold ammine complexes,[10] and surface functionalisation with amine or thiol groups.[11–13] However, these interactions often alter the electronic state of the Au particles to a considerable degree.[14,15] Consequently, examples of highly zero-valent, finely dispersed Au being applied as a catalyst are rare. Nonetheless, several studies have demonstrated that even zero-valent Au can exhibit catalytic activity for processes such as glucose oxidation.[16,17] Moreover, in partially oxidised catalysts, metallic Au(0) is known to play a pivotally important role as a catalyst for the activation of reactive oxygen species.[4,18]

Therefore, the development of silica-based catalysts that support highly dispersed, zero-valent Au particles is important as a foundational platform for designing catalysts that utilise the Au(0) state effectively, or which allow tunability of the Au charge state.

To address the challenge of achieving high dispersion and stabilisation of Au(0) nanoparticles, a promising approach involves molecular-level structural control using siloxane-based building blocks. This bottom-up synthesis enables the uniform introduction of functional groups, facilitating the design of advanced silica materials with tailored cage-type oligosiloxanes D*n*R (n = 4, 6 and 8) offering thermal and chemical stability, with tunable vertices for diverse functionalization.[19–23] Additionally, their use as precursors for synthesising porous materials has been reported.[23–25] They are promising building blocks for silica-based porous materials. Particularly, D4R, a secondary structural unit of LTA zeolites,[26] holds potential for the synthesis of robust porous supports.

[a]*Department of Applied Chemistry, Faculty of Science and Engineering, Waseda University, 3-4-1 Okubo, Shinjuku-ku, Tokyo 169-8555, Japan. E-mail: ysekine@waseda.jp*
[b]*Department of Applied Chemistry, Faculty of Science and Engineering, Chuo University, 1-13-27 Kasuga, Bunkyo-ku, Tokyo 112-8551, Japan*
[c]*Kagami Memorial Research Institute for Materials Science and Technology, Waseda University, 2-8-26 Nishiwaseda, Shinjuku-ku, Tokyo 169-0051, Japan*
[d]*Waseda Research Institute for Science and Engineering, Waseda University, 3-4-1 Okubo, Shinjuku-ku, Tokyo 169-8555, Japan*

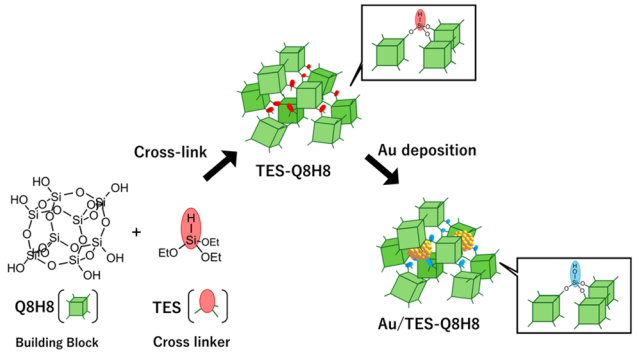

Scheme 1 The synthesis of **TES-Q8H8** and deposition of Au NPs.

This report describes the synthesis of a novel silica-based porous support using cage siloxanes as building blocks, designed to achieve high dispersion and confinement of Au nanoparticles, thereby suppressing agglomeration.

We crosslinked D4R-type cage siloxane, Q8H8, with triethoxysilane (TES) (Scheme 1). The hydrosilyl groups present in triethoxysilane can reduce noble metal salts, as shown in eqn (1). The groups reportedly facilitate on-site reduction and deposition of metallic species on monolithic structures.[27]

$$n\mathrm{O}_{1.5}\mathrm{Si}-\mathrm{H}+\mathrm{Me}^{n+}+n\mathrm{H}_2\mathrm{O}\rightarrow n\mathrm{O}_{1.5}\mathrm{Si}-\mathrm{OH}+\mathrm{Me}(0)+n/2\mathrm{H}_2+n\mathrm{H}^{+}\quad(\mathrm{Me}^{n+}=\mathrm{Ag}^{+},\ \mathrm{Pd}^{2+},\ \mathrm{Au}^{3+},\ \text{and}\ \mathrm{Pt}^{4+}) \tag{1}$$

Additionally, silanol groups generated from the oxidation of hydrosilyl groups can undergo condensation to form siloxane bonds,[28] potentially enhancing aggregation resistance through structural stabilisation and producing the expected higher selectivity for several reactions.[29,30]

Herein, we describe the synthesis of silica-based porous materials featuring hydrosilyl-functionalized D4R frameworks and the use of these materials to achieve on-site reduction, dispersion, and confinement of Au(0) nanoparticles, along with their aggregation-suppression effects.

Experimental

Materials

The following chemicals were used without further purification: tetraethoxysilane (TEOS, ≥95.0%; Fujifilm Wako Pure Chemical Corp.), triethoxysilane (TES; Enamine Ltd) tetramethylammonium hydroxide pentahydrate (TMAOH-5H_2O, ≥95.0%; Aldrich Chemical Co. Inc.), ethanol (EtOH, ≥99.5%; Fujifilm Wako Pure Chemical Corp.), tetrahydrofuran (THF, ≥99.5%, Stabilizer Free; Fujifilm Wako Pure Chemical Corp.), magnesium sulphate ($MgSO_4$, ≥98.0%; Fujifilm Wako Pure Chemical Corp.), nitric acid (1.42) (HNO_3; Fujifilm Wako Pure Chemical Corp.), *N*,*N*-dimethylacetamide (DMAc, ≥99.0%; Hayashi Pure Chemical Ind. Ltd), hydrochloric acid (HCl; Fujifilm Wako Pure Chemical Corp.), hydrogen tetrachloroaurate(III) tetrahydrate ($HAuCl_4$-4H_2O, >99.9%; Kanto Chemical Co. Inc.).

Preparation of TES-Q8H8

The building block, **Q8H8**, $Si_8O_{12}(OH)_8$, dispersed in a mixture of THF and DMAc was obtained after acid treatment and subsequent dehydration by $MgSO_4$ of $TMA_8(Si_8O_{20})$ after using a method reported earlier.[31] Then, **Q8H8** was reacted with HSi$(OEt)_3$ to obtain a porous material. Specifically, 135 mL of Q8H8 solution in THF and 5.212 ml of HSi$(OEt)_3$ were mixed at a molar ratio of 3 : 8, ensuring stoichiometric amounts of silanol groups and ethoxy groups. The mixture was refluxed at 353 K for 1 day under a N_2 atmosphere. After a white solid was precipitated in the solution, it was filtered with THF and dried under reduced pressure to obtain a slightly lumpy white powder. The powder was stirred in EtOH for 1 h to remove residual DMAc. Then it was filtered and dried under reduced pressure, yielding a smooth white powder designated as **TES-Q8H8**.

Deposition of Au particles on TES-Q8H8 and its calcination

Au particles were deposited onto/into **TES-Q8H8** through the redox reaction of hydrosilyl groups and Au^{3+} ions. A small amount of water was used to disperse **TES-Q8H8**, with subsequent addition of a tetrachloroauric(III) acid solution equivalent to 5 wt%. The mixture was stirred for 1 day under light shielding. After filtration with water and drying under reduced pressure, a dark purple powder was obtained, denoted as **Au/TES-Q8H8**. The sample was then calcined in air at 773 K for 1 h to yield a dark purple powder, designated as **Au/TES-Q8H8-calc**.

Acid treatment of Au-supported TES-Q8H8

Au/TES-Q8H8 and **Au/TES-Q8H8-calc**. were stirred in a mixture of 15 mL nitric acid and 5 mL hydrochloric acid for 5 min. The solution was then diluted with water immediately while cooling in an ice bath. Subsequently, the process was repeated several times, involving centrifugation and decantation. The resulting precipitate was dried under reduced pressure, yielding white to light purple powders, designated respectively as **Au/TES-Q8H8-acid** and **Au/TES-Q8H8-calc.-acid**.

Characterization

Liquid-state ^{1}H, ^{13}C and ^{29}Si nuclear magnetic resonance (NMR) spectra were recorded using a spectrometer (JNM ECZ500R; JEOL) with resonance frequencies of 500.16, 125.77, and 99.37 MHz, respectively, at room temperature using 5 mm glass tubes. Acetone-d_6 was used to obtain lock signals. Tetramethylsilane (δ = 0 ppm) was used as the internal reference. Tetraethylsilane (δ = 5.75 ppm) was used to quantify the Si concentration in solutions of the samples for liquid-state ^{29}Si NMR spectroscopy. A small amount of Cr(acac)$_3$ (acac = acetylacetonate) was used as a relaxation agent for the ^{29}Si nuclei. Liquid-state ^{29}Si NMR spectra were measured using a 45° pulse and recycle delay of 10 s. Solid-state ^{29}Si magic angle spinning (MAS) NMR spectra were recorded on a spectrometer

(JNM-ECA400; JEOL) at a resonance frequency of 79.43 MHz with a 90° pulse and pulse delay of 250 s at ambient temperature. Solid-state ^{13}C cross-polarization (CP)/MAS NMR spectra were recorded on the same spectrometer at a resonance frequency of 100.53 MHz with a contact time of 5 ms and pulse delay of 5 s. The samples were put in a 5 mm zirconia rotor and were spun at 8 kHz. Hexamethylbenzene was used as an external reference (δ = 17.4 ppm) for solid-state ^{13}C NMR spectroscopy. Poly(dimethylsilane) was used as an external reference (δ = −33.8 ppm) for solid-state ^{29}Si NMR spectroscopy. Solid-state two-dimensional ^{1}H–^{29}Si heteronuclear correlation solid-state (HETCOR) NMR spectra were recorded using the same spectrometer at resonance frequencies of 400.0 MHz for ^{1}H and 79.4 MHz for ^{29}Si with contact time of 5 ms. Fourier transform infrared (FT-IR) spectra were obtained using a spectrometer (FT/IR-6100; Jasco Corp.) with the KBr method. Powder X-ray diffraction (XRD) patterns were obtained using a diffractometer (Smart Lab; Rigaku Corp.) employing CuKα radiation (40 kV, 40 mA). Also, N_2 adsorption–desorption measurements were performed with a at 77 K (Autosorb-iQ; Quantachrome Instruments). As pretreatments, the samples were heated at 393 K for 4.5 h under reduced pressure. Brunauer–Emmett–Teller (BET)[32] areas were calculated using the Rouquerol method.[33] Transmission electron microscopy (TEM) images were taken using a microscope (JEM-2100F; JEOL) operating at 200 kV. Energy dispersive X-ray spectra (EDXS) mapping was done (JED-2300T; JEOL). X-ray photoelectron spectroscopy (XPS) measurements were taken (VersaProbe 4; ULVAC-PHI) under vacuum conditions. The depth profiles of samples were obtained using an argon gas cluster ion beam with energy of 4 kV. Au L3-edge X-ray absorption fine structure (XAFS) analyses were conducted at the beamline BL14B2 of SPring-8 at the Japan Synchrotron Radiation Research Institute. The X-rays were monochromatized using a Si(311) double-crystal monochromator. The photon energy was calibrated at the inflection point of the Au L3-edge X-ray absorption near-edge structure (XANES) spectrum (pre-edge peak) of the Au metal foil to 11 921.7 eV.[34] The powdered samples were diluted with boron nitride (BN), pressed into pellets in a metal holder, and used for X-ray absorption spectroscopy (XAS) measurements. Inductively coupled plasma (ICP, 5100 ICP-OES; Agilent Technologies Inc.) analysis was conducted. For ICP analysis, the samples were dissolved in a mixture of hydrofluoric acid and aqua regia.

Results and discussion

Synthesis of TES-Q8H8

FT-IR spectra of **TES-Q8H8** and $TMA_8(Si_8O_{20})$ are presented in Fig. 1(a). **TES-Q8H8** showed distinctive bands at 1080 cm^{-1} and a shoulder peak at 1150 cm^{-1} (Fig. 1(b)), assignable to $(Si–O)_4$ ring-symmetry/asymmetry mode respectively.[35] The bands indicate the D4R structures remain even after cross-linking. Bands observed at 881 and 2264 cm^{-1} are presumably derived respectively from Si–H bending and stretching vibrations.

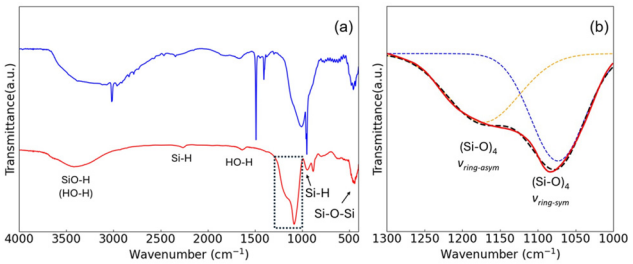

Fig. 1 (a) FT-IR spectra of $TMA_8(Si_8O_{20})$ (blue) and **TES-Q8H8** (red). (b) Enlarged image of FT-IR spectra near 1000–1300 cm^{-1} for **TES-Q8H8**. Orange and blue dashed lines show the fitted peaks for the asymmetric and symmetric modes of $(Si–O)_4$ rings, respectively. The black dashed line in (b) represents the combined fitting curve.

Then they represent the existence of hydrosilyl groups.[35,36] These results support that **TES-Q8H8** has properties of both TES and Q8H8. The broad band of **TES-Q8H8** at 3000–3700 cm^{-1} can be assigned to the SiO-H vibration of silanol groups.[37] Although the HO-H weak band observed at 1634 cm^{-1} indicates the existence of the adsorbed water molecules,[37–39] the presence of a shoulder peak around 3700 cm^{-1}, attributed to isolated silanol groups, provides evidence for the existence of silanol.[36,37]

The existence of hydrosilyl groups in **TES-Q8H8** was confirmed further by TGA measurements (Fig. S1). The slight increase in weight observed over 673 K for **TES-Q8H8** provides a reasonable explanation for the oxidation of SiH groups.[36,40]

The solid-state ^{29}Si MAS NMR spectra of **TES-Q8H8** in Fig. 2(a) showed signals attributed to T^2(**Si**HOEt$(OSi)_2$ and/or **Si**HOH$(OSi)_2$), T^3(**Si**H$(OSi)_3$), Q^3(**Si**OH$(OSi)_3$), and Q^4(**Si**$(OSi)_4$) sites, respectively at −74.09, −83.61, −99.40, and −108.22 ppm. The integrated intensity ratio of $(Q^3 + Q^4)/(T^2 + T^3)$ was 2.78, which was similar to the theoretical ratio (Q/T = 3), implying that the stoichiometric reaction proceeded, whereas T^2 and Q^3 respectively illustrate the existence of uncross-linked parts of TES and Q8H8. Taking this supposition into consideration, we can calculate the ratio of cross-linked parts of triethoxysilane with $Q^4/(3T^3 + 2T^2)$ (theoretical ratio is 1) and the ratio of cross-linked parts of Q8H8 with $Q^4/(Q^4 + Q^3)$. Experimentally obtained results show the ratio of $Q^4/(3T^3 + 2T^2)$ as 0.603 and

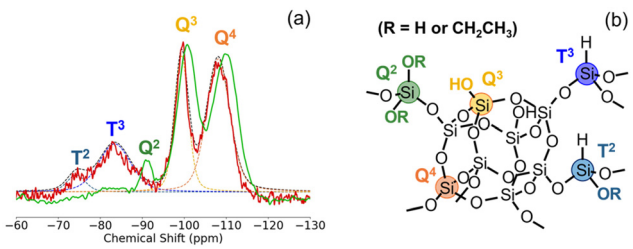

Fig. 2 (a) Solid-state ^{29}Si MAS NMR spectra of **TES-Q8H8** (red) and **Au/TES-Q8H8** (green). Pale blue, blue, yellow and orange dotted lines respectively represent fitting data of **TES-Q8H8** attributable to T^2, T^3, Q^3, and Q^4 environments. (b) Si environment in the assumed structure of **TES-Q8H8**.

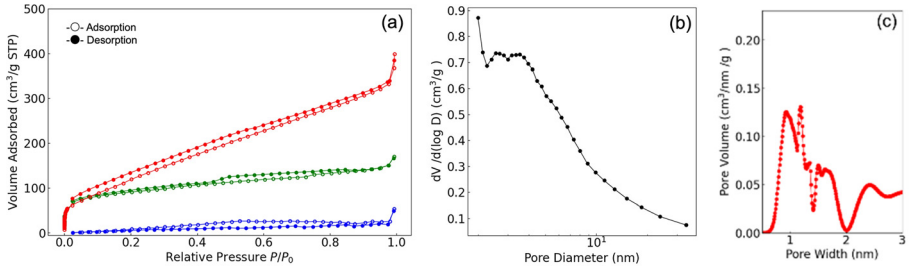

Fig. 3 (a) N_2 adsorption–desorption isotherms of **TES-Q8H8** (red), **Q8H8-only** (blue), and **TES-Q8H8-calc.** (green). (b) Pore size distribution, as determined from BJH analysis of Adsorption data for **TES-Q8H8**. (c) Micro pore size distribution determined from SF analysis of **TES-Q8H8**.

that of $Q^4/(Q^4 + Q^3)$ as 0.632: the difference between them was estimated as the result of condensation between Q8H8. In addition, when comparing the area ratios of the T^2 and Q^3 signals corresponding to the uncross-linked parts, the ratio of Q^3/T^2 was 12.0. These results imply that cross-linking occurred between triethoxysilanes, whereas almost no cross-linking between Q8H8 was observed.

The N_2 adsorption–desorption isotherm of **TES-Q8H8** (Fig. 3(a)) appeared to be combined Type I and Type II of the IUPAC classification with the Brunauer–Emmett–Teller (BET)[33] area of 510 m^2 g^{-1} and total pore volume of 0.52 cm^3 g^{-1}. However, when Q8H8 was refluxed without TES and was subjected to the same treatment, a white powder denoted as **Q8H8-only** was produced, with much smaller BET area (76 m^2 g^{-1}) and total pore volume (0.038 cm^3 g^{-1}) than those of **TES-Q8H8**. Furthermore, when TES without Q8H8 was refluxed at 353 K, a much smaller amount of solid was obtained. These results indicate that cross-linking of Q8H8 using the appropriate linker is necessary to achieve high porosity. Furthermore, pore-size distributions calculated using the Barrett–Joyner–Halenda (BJH) method show that **TES-Q8H8** mainly has mesopores with diameters less than 10 nm (Fig. 3(b)),[32] and the Saito–Foley (SF)[41] method shows micro-pore size distribution. The surface area and pore volume of **TES-Q8H8**-based materials are summarized in Table S1.

In situ reduction of Au^{3+} ion in TES-Q8H8

Fig. 2(a) shows ^{29}Si MAS NMR spectra of **Au/TES-Q8H8**. The Si environment of **Au/TES-Q8H8** differs from **TES-Q8H8** in that T signals have diminished. These results indicate that the oxidation of hydrosilyl groups across **Au/TES-Q8H8** proceeded. The Q^2 signal in **Au/TES-Q8H8** can be attributed to the partial cleavage of D4R structures and/or triethoxysilane-derived cross-linkers.

The N_2 adsorption–desorption isotherm shows that **Au/TES-Q8H8** has a smaller BET area (409 m^2 g^{-1}) and pore volume (0.33 cm^3 g^{-1}) than those of **TES-Q8H8** (Fig. S2). This difference is probably attributable to the incorporation of Au particles and/or possible partial rearrangement of the porous structure.[13]

The amount of Au for **Au/TES-Q8H8** obtained by ICP-OES was 2.11 wt%. Showing the existence of Au after immersing **TES-Q8H8** with the solution of $HAuCl_4$.

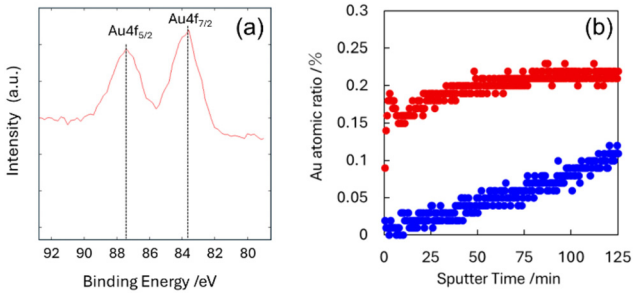

Fig. 4 (a) XPS spectra of **Au/TES-Q8H8** before argon sputtering. (b) Atomic ratio of Au in **Au/TES-Q8H8** (red) and **Au/TES-Q8H8-calc.-acid** (blue) with argon sputtering.

X-ray photoelectron spectroscopy (XPS) measurement of **Au/TES-Q8H8** detected $Au4f_{7/2}$ and $Au4f_{5/2}$ photoelectron signals respectively at around 84 and 88 eV (Fig. 4(a)),[42] also showing the existence of Au in **Au/TES-Q8H8**. We note that the surface charging effect could not be excluded for this material,[10,43] which might have led to deviations in the measured binding energies. Therefore, the electric state of Au was not quantified with XPS. The percentage of Au considering Au, O, and Si in **Au/TES-Q8H8** was 0.17 mol% for the first ten cycles on average, which remained almost constant (0.21 mol%) for the last ten cycles on average after 250 argon sputter cycles at 30 s per cycle (Fig. 4(b)).

X-ray absorption fine structure (XAFS) measurements were taken to investigate the electronic states of Au particles in **Au/TES-Q8H8**. Au L3-edge X-ray absorption near edge structure (XANES) spectra (Fig. S3(a)) of **Au/TES-Q8H8** show much less intense pre-edge peaks for **Au/TES-Q8H8** and correspond well with those of Au foil. These spectra indicated that Au in **Au/TES-Q8H8** was mostly Au(0). In this regard, Au^{3+} was surely reduced in the inner part of **Au/TES-Q8H8**.

Scanning transmission electron microscope (STEM) images of **Au/TES-Q8H8** in Fig. 5(a) and energy dispersive X-ray spectrometry (EDS) mapping in Fig. 5(b) reveal the presence of supported Au nanoparticles across the entire support. However, some particles larger than 10 nm in diameter were observed. Fig. 5(c) shows that such larger Au particles are distributed mainly on the **Au/TES-Q8H8** surface: a phenomenon often

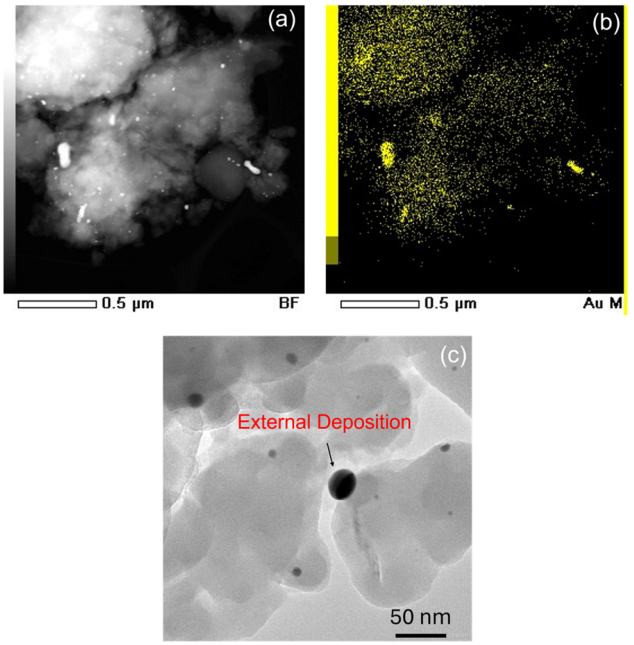

Fig. 5 (a) STEM image of **Au/TES-Q8H8**, (b) STEM-EDS mapping of **Au/TES-Q8H8**, and (c) TEM images of **Au/TES-Q8H8**.

seen in Au deposition on porous materials.[11] This finding is consistent with the pore size distribution of **TES-Q8H8**.

The XRD patterns of **TES-Q8H8** and **Au/TES-Q8H8** are presented in Fig. S4. The appearance of diffraction peaks derived from Au(JCPDS#04-0784) was observed after immersion of **TES-Q8H8** with $HAuCl_4$ solution, and the average Au particle radius calculated from Scherrer's equation was 25.4 nm. This is even larger than the radii of externally supported Au particles observed in TEM images. This discrepancy is presumably due to the pre-treatment of TEM measurement. The TEM samples were prepared using the supernatant obtained after dispersing the powders in ethanol, suggesting that the larger externally supported particles may have sedimented during stirring. The corresponding XRD results of the sample after removing these externally supported particles are discussed later.

Therefore, removing surface-located Au particles is crucially important for not only achieving a more uniform distribution of Au nanoparticles throughout the material but also the analysis of the properties for confined Au particles.

Information on the Au loading and average particle size of **Au/TES-Q8H8**-based materials is summarized in Table S2.

Calcination of Au-supported TES-Q8H8

To investigate resistance to agglomeration, the calcination process was applied to **Au/TES-Q8H8** and was designated as **Au/TES-Q8H8-calc**. Usually, metal species agglomerate as heating proceeds according to the Ostwald ripening model mechanism.[44,45] However, Au particle distributions from TEM images show that the average radius of Au particles was almost identical after calcination, although the number of Au particles smaller than 5 nm decreased (Fig. 6(a) and (b)). These results suggest that some agglomerated Au particles might have been redispersed during the calcination process, thereby contributing to the maintenance of average particle size.[45] Qian *et al.* reported that redispersion of Au particles occurs when the Au/SiO_2 is calcined.[46] In their research, the particle size distribution, which was uniform before calcination, became broader after calcination, leading to highly dispersed smaller Au particles. Simultaneously, large Au particles were also produced. By contrast, the absence of larger Au particles after calcination in this study is likely attributable to the suppression of agglomeration by the confinement effect of Au particles in the porous silica network.

The 2D ^1H-^{29}Si CP/MAS NMR HETCOR spectra of **Au/TES-Q8H8** and **Au/TES-Q8H8-calc**. show calcination effects as presented in Fig. S5(a) and (b). One typical change was diminishment of the Q^2 signal. Because this signal is apparent in short contact time spectra of **Au/TES-Q8H8** (Fig. S5(c)), silanol groups in proximity likely underwent condensation, forming Si–O–Si linkage.[47] The indistinguishable broadened Q^3 and Q^4 signals represent various Si–O–Si and Si-OH environments.

To confirm that reduction of Au^{3+} occurs by the hydrosilyl groups in **TES-Q8H8**, **TES-Q8H8** heated in air for one hour before impregnation is hereinafter designated as **TES-Q8H8-calc**. This **TES-Q8H8-calc**. was found to retain its microporosity (Fig. 3(a)). The impregnation of **TES-Q8H8-calc**. with $HAuCl_4$ solution for 1 day yields a white powder designated as **TES-Q8H8-calc.-Au**. TEM images confirm the near lack of Au particles in **TES-Q8H8-calc.-Au**. The loading amount of Au obtained by ICP-OES was 0.032 wt%. These results indicate that deposition of Au inside **TES-Q8H8** was driven by the reduction of hydrosilyl groups.

Acid treatment of Au/TES-Q8H8 and Au/TES-Q8H8-calc.

Au/TES-Q8H8 and **Au/TES-Q8H8-calc**. were treated with acid for the removal of externally supported Au particles. The Au loading on **Au/TES-Q8H8-acid** was 0.0029 wt%, indicating that Au particles across **Au/TES-Q8H8** were leached out after the treatment. By contrast, not all Au was leached out for the calcined samples **Au/TES-Q8H8-calc.-acid**, with loading of

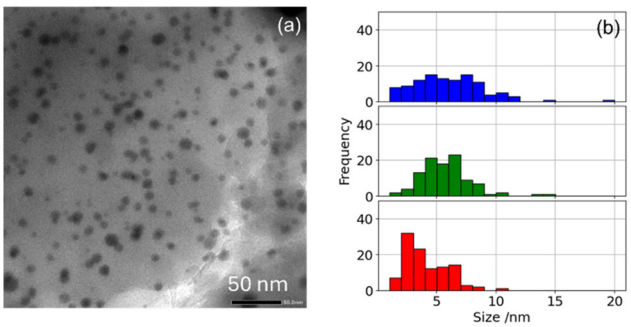

Fig. 6 (a) TEM images of **Au/TES-Q8H8-calc**. and (b) Au particle distribution of **Au/TES-Q8H8** (blue), **Au/TES-Q8H8-calc**. (green) and **Au/TESQ8H8-calc.-acid** (red).

0.22 wt%. The **Au/TES-Q8H8-calc.-acid** depth profile presented in Fig. 4(b) shows almost no Au deposition on the **Au/TES-Q8H8-calc.-acid** surface. However, as the sputter cycles progressed, more Au was detected in **Au/TES-Q8H8-calc.-acid**. Furthermore, the XRD analysis of **Au/TES-Q8H8-calc.-acid** in Fig. S2 revealed that the diffraction peak corresponding to the Au(111) plane became weaker and broader than **Au/TES-Q8H8**. Based on the Scherrer equation, the average particle size of Au was estimated to be 7.1 nm. Taking into account that this equation reflects a volume-weighted average of particle sizes,[48] the result is consistent with the particle size distribution in Fig. 6(b).

Considering the dehydration–condensation occurring between silanol groups during the calcination process, one can reasonably infer that the Au particles were confined within the support.

Conclusions

We have synthesised a new porous silica (**TES-Q8H8**) using cage siloxane as a building block. Hydrosilyl groups introduced throughout the **TES-Q8H8** structure enabled the support of Au particles by immersion with chloroauric acid (**Au/TES-Q8H8**). The Au particles in a metallic state were uniformly supported on the whole material. Some particles were deposited as large particles on the surface. However, they were removable by acid treatment. Even after calcination of **Au/TES-Q8H8** at 773 K for 1 h, the average Au particle size of **Au/TES-Q8H8** changed only slightly. An effect of confinement was observed. In addition, **Au/TES-Q8H8** after calcination showed improved resistance to acid treatment, indicating that the Au particle confinement had improved. This new material is expected to be applied as a newly porous silica-based catalyst.

Conflicts of interest

There are no conflicts to declare.

Data availability

The data supporting this article have been included in the manuscript itself and in the SI. Supplementary information is available. See DOI: https://doi.org/10.1039/d5dt01824b.

Acknowledgements

The author expresses sincere gratitude to Dr Taiki Hayashi for his valuable advice and support in initiating this research. Appreciation is also extended to Ms Madoka Chino for her assistance with various aspects of the experiments, Mr Koki Saegusa for his invaluable help in establishing the experimental environment, and Dr Ayaka Shigemoto for her constructive suggestions related to the experimental work. The author also thanks Dr Takuma Higo and Mr Hiromu Akiyama for their cooperation with XPS and XAFS measurements, and Mr Kosuke Watanabe for his assistance in setting up the TGA system. This work benefited from research equipment shared in the MEXT Project for Promoting Public Utilization of Advanced Research Infrastructure (Program for Supporting Construction of Core Facilities, Grant Number JPMXS0440500023). A part of this work was supported by JSPS KAKENHI Grant Numbers 23H05404, 24H00487, and 23K20034.

References

1 M. Haruta, T. Kobayashi, H. Sano and N. Yamada, *Chem. Lett.*, 1987, **16**, 405–408.
2 G. J. Hutchings, *J. Catal.*, 1985, **96**, 292–295.
3 B. Hvolbæk, T. V. W. Janssens, B. S. Clausen, H. Falsig, C. H. Christensen and J. K. Nørskov, *Nano Today*, 2006, **2**, 14–18.
4 T. Ishida, T. Murayama, A. Taketoshi and M. Haruta, *Chem. Rev.*, 2020, **120**, 464–525.
5 G. Kennedy, L. R. Baker and G. A. Somorjai, *Angew. Chem., Int. Ed.*, 2014, **53**, 3405–3408.
6 Y. Wei, W. Yang and Z. Yang, *Int. J. Hydrogen Energy*, 2022, **47**, 9537–9565.
7 C. S. Ewing, G. Veser, J. J. McCarthy, D. S. Lambrecht and J. K. Johnson, *Surf. Sci.*, 2016, **652**, 278–285.
8 C. Pan, M. Tsai, W. Su, J. Rick, N. G. Akalework, A. K. Agegnehu, S. Cheng and B. Hwang, *J. Taiwan Inst. Chem. Eng.*, 2017, **74**, 154–186.
9 J. P. Gabaldon, M. Bore and A. K. Datye, *Top. Catal.*, 2007, **44**, 253–262.
10 F. Somodi, I. Borbáth, M. Hegedűs, A. Tompos, I. E. Sajó, Á. Szegedi, S. Rojas, J. L. G. Fierro and J. L. Margitfalvi, *Appl. Catal., A*, 2008, **347**, 216–222.
11 P. R. Selvakannan, K. Mantri, J. Tardio and S. K. Bhargava, *J. Colloid Interface Sci.*, 2013, **394**, 475–484.
12 Y. Ma, G. Nagy, M. Siebenbürger, R. Kaur, K. M. Dooley and B. Bharti, *J. Phys. Chem. C*, 2022, **126**, 2531–2541.
13 E. Eom, M. Song, J. C. Kim, D. Kwon, D. N. Rainer, K. Gołąbek, S. C. Nam, R. Ryoo, M. Mazur and C. Jo, *JACS Au*, 2022, **2**, 2327.
14 R. Schürmann, E. Titov, K. Ebel, S. Kogikoski, A. Mostafa, P. Saalfrank and A. R. Milosavlijević, *Nanoscale Adv.*, 2022, **4**, 1599–1607.
15 Y. Zhang, J. Zhang, B. Zhang, R. Si, B. Han, F. Hong, Y. Niu, L. Sun, L. Li, B. Qiao, K. Sun, J. Huang and M. Haruta, *Nat. Commun.*, 2020, **11**, 558.
16 Y. Mikami, A. Dhakshinamoorthy, M. Alvaro and H. García, *Catal. Sci. Technol.*, 2013, **3**, 58–69.
17 M. Comotti, C. D. Prina, E. Falletta and M. Rossi, *Adv. Synth. Catal.*, 2006, **348**, 313–316.
18 G. Corro, S. Cebada, U. Pal and J. L. G. Fierro, *J. Catal.*, 2017, **347**, 148–153.
19 A. Shimojima and K. Kuroda, *Molecules*, 2020, **25**, 524.

20 D. B. Cordes, P. D. Lickiss and F. Rataboul, *Chem. Rev.*, 2010, **110**, 2081–2173.
21 T. Hikino, K. Fujino, N. Sato, H. Wada, K. Kuroda and A. Shimojima, *Chem. Lett.*, 2021, **50**, 1643–1647.
22 S. Saito, H. Wada, A. Shimojima and K. Kuroda, *Inorg. Chem.*, 2018, **57**, 14686–14691.
23 T. Nishitoba, T. Matsumoto, F. Yagihashi, J. Satou, T. Kikuchi, K. Sato and M. Igarashi, *Chem. Mater.*, 2024, **36**, 10198–10204.
24 N. Sato, Y. Kuroda, H. Wada, A. Shimojima and K. Kuroda, *Chem. – Eur. J.*, 2018, **24**, 17033–17038.
25 T. Hayashi, T. Matsuno, K. Kuroda and A. Shimojima, *Chem. Lett.*, 2024, **53**, upae025.
26 C. S. Cundy and P. A. Cox, *Chem. Rev.*, 2003, **103**, 663–702.
27 N. Moitra, K. Kanamori, T. Shimada, K. Takeda, Y. H. Ikuhara, X. Gao and K. Nakanishi, *Adv. Funct. Mater.*, 2013, **23**, 2714–2722.
28 N. Sato, Y. Kuroda, T. Abe, H. Wada, A. Shimojima and K. Kuroda, *Chem. Commun.*, 2015, **51**, 11034–11037.
29 Y. Zhang, R. Takahashi, K. Kimura, H. Fujitsuka and T. Tago, *Catal. Surv. Asia*, 2023, **27**, 56–66.
30 C. Wang, L. Wang, J. Zhang, H. Wang, J. P. Lewis and F. S. Xiao, *J. Am. Chem. Soc.*, 2016, **138**, 7880–7883.
31 M. Igarashi, T. Nozawa, T. Matsumoto, F. Yagihashi, T. Kikuchi and K. Sato, *Nat. Commun.*, 2021, **12**, 7025.
32 S. Brunauer, P. H. Emmett and E. Teller, *J. Am. Chem. Soc.*, 1938, **60**, 309–319.
33 J. Rouquerol, P. Llewellyn and F. Rouquerol, *Stud. Surf. Sci. Catal.*, 2007, **160**, 49–56.
34 H. Asakura, S. Yamazoe, T. Misumi, A. Fujita, T. Tsukuda and T. Tanaka, *Radiat. Phys. Chem.*, 2020, **175**, 108270.
35 E. S. Park, H. W. Ro, C. V. Nguyen, R. L. Jaffe and D. Y. Yoon, *Chem. Mater.*, 2008, **20**, 1548–1554.
36 M. Marrone, T. Montanari, G. Busca, L. Conzatti, G. Costa, M. Castellano and A. Turturro, *J. Phys. Chem. B*, 2004, **108**, 3563–3572.
37 E. A. Paukshtis, M. A. Yaranova, I. S. Batueva and B. S. Bal'zhinimaev, *Microporous Mesoporous Mater.*, 2019, **288**, 109582.
38 S. P. Zhdanov, L. S. Koshelev and T. I. Titova, *Langmuir*, 1987, **3**, 960–967.
39 A. Burneau and O. Barrès, *Langmuir*, 1990, **6**, 1364–1372.
40 T. Shioda, T. Gunji, N. Abe and Y. Abe, *Appl. Organomet. Chem.*, 2011, **25**, 661–664.
41 A. Saito and H. C. Foley, *AIChE J.*, 1991, **37**, 429–437.
42 N. Kruse and S. Chenakin, *Appl. Catal., A*, 2011, **391**, 367–376.
43 A. Pélisson-Schecker, H. J. Hug and J. Patscheider, *Surf. Interface Anal.*, 2011, **44**, 29–36.
44 P. W. Voorhees, *J. Stat. Phys.*, 1985, **38**, 231–252.
45 L. Liu, J. Lu, Y. Yang, W. Ruettinger, X. Gao, M. Wang, H. Lou, Z. Wang, Y. Liu, X. Tao, L. Li, Y. Wang, H. Li, H. Zhou, C. Wang, Q. Luo, H. Wu, K. Zhang, J. Ma, X. Cao, L. Wang and F. Xiao, *Science*, 2023, **383**, 94–101.
46 K. Qian, Z. Jiang and W. Huang, *J. Mol. Catal. A: Chem.*, 2007, **264**, 26–32.
47 S. Smeets, Z. J. Berkson, D. Xie, S. I. Zones, W. Wan, X. Zou, M.-F. Hsieh, B. F. Chmelka, L. B. McCusker and C. Baerlocher, *J. Am. Chem. Soc.*, 2017, **139**, 16803–16812.
48 C. Weidenthaler, *Nanoscale*, 2011, **3**, 792–810.